Full paper

Coulomb drag and counterflow Seebeck coefficient in bilayer-graphene double layers

J. Hu[a,b,d,e,*], T. Wu[b,c], J. Tian[b,c], N.N. Klimov[d,e], D.B. Newell[d], Y.P. Chen[a,b,c,*]

[a] School of Electrical and Computer Engineering, Purdue University, West Lafayette, IN 47907, USA
[b] Birck Nanotechnology Center, Purdue University, West Lafayette, IN 47907, USA
[c] Department of Physics and Astronomy, Purdue University, West Lafayette, IN 47907, USA
[d] Physical Measurement Laboratory, National Inistitute of Standards and Technology, Gaithersburg, MD 20899, USA
[e] Joint Quantum Institute, University of Maryland, College Park, MD 20742, USA

ARTICLE INFO

ABSTRACT

We have fabricated bilayer-graphene double layers separated by a thin (~ 20 nm) boron nitride layer and performed Coulomb drag and counterflow thermoelectric transport measurements. The measured Coulomb drag resistivity is nearly three orders smaller in magnitude than the intralayer resistivities. The counterflow Seebeck coefficient is found to be well approximated by the difference between Seebeck coefficients of individual layers and exhibit a peak in the regime where two layers have opposite sign of charge carriers. The measured maximum counterflow power factor is ~ 700 μW/K^{2}cm at room temperature, promising high power output per mass for lightweight thermoelectric applications. Our devices open a possibility for exploring the novel regime of thermoelectrics with tunable interactions between n-type and p-type channels based on graphene and other two-dimensional materials and their heterostructures.

1. Introduction

Graphene and boron nitride (BN) based heterostructures have attracted intense attention in recent years [1–5]. With the flake transfer technique [6,7,1,2] that enables convenient stacking of a large variety of two-dimensional layered materials, high quality samples of graphene/BN/graphene (where the BN thickness can be as thin as down to ~ 1 nm [8]) and other heterostructures have been fabricated to study the interlayer interactions. For example, strong Coulomb drag [8–10] and tunable metal-insulator transition [11] have been observed. Vertical field-effect transistor [12] and resonant tunneling [13,14] using atomically thin barriers have been demonstrated, promising for applications in logic and high-frequency devices. The electron-hole symmetry allows each layer of graphene to be populated with electrons or holes using gates, which is usually difficult to achieve in traditional semiconductor quantum wells [15]. In the regime where one graphene layer is p-type while the other is n-type, the intriguing exciton condensation [16] has been predicted, though the predicted transition temperature spans a wide range [17–26]. A recent proposal suggests that in bilayer-graphene (BLG) double layers, the transition temperature could be well above liquid helium temperatures at zero magnetic field [25]. This novel phase transition can be detected by performing counterflow transport (with equal magnitude and opposite direction of

current in two layers), Coulomb drag and other measurements [16,27]. An anomalous negative Coulomb drag is observed in BLG double layers [9,10], which is different from the drag in monolayer graphene double layers [28,8]. Signatures of exciton superfluid have been recently observed in BLG in magnetic field with much higher transition temperature than that in double quantum wells [29,30,16]. In addition, thermoelectric transport is a powerful tool for studying not only the single particle transport [31], but also strongly correlated systems [32,33] and macroscopic quantum coherence [34–36] such as exciton condensation. Thermoelectric transport might also be relevant to understanding the drag measurements in BLG double layers [9]. Nevertheless, no counterflow thermoelectric transport measurements have been performed.

As another motivation for the current work, high efficiency thermoelectric modules have been pursued for decades to improve solid-state thermoelectric generators and Peltier refrigerators. Due to often conflicting parameters, producing such modules requires careful material and structural engineering [37]. High thermoelectric efficiency in low dimensional and nano-materials has been demonstrated, particularly for "electron-crystal-phonon-glass" systems that have high electrical conductivity and low thermal conductivity [38,37]. These traditional approaches focus on engineering the properties of a given material to enhance the thermoelectric figure of merit $ZT = \frac{\sigma S^2 T}{\kappa}$,
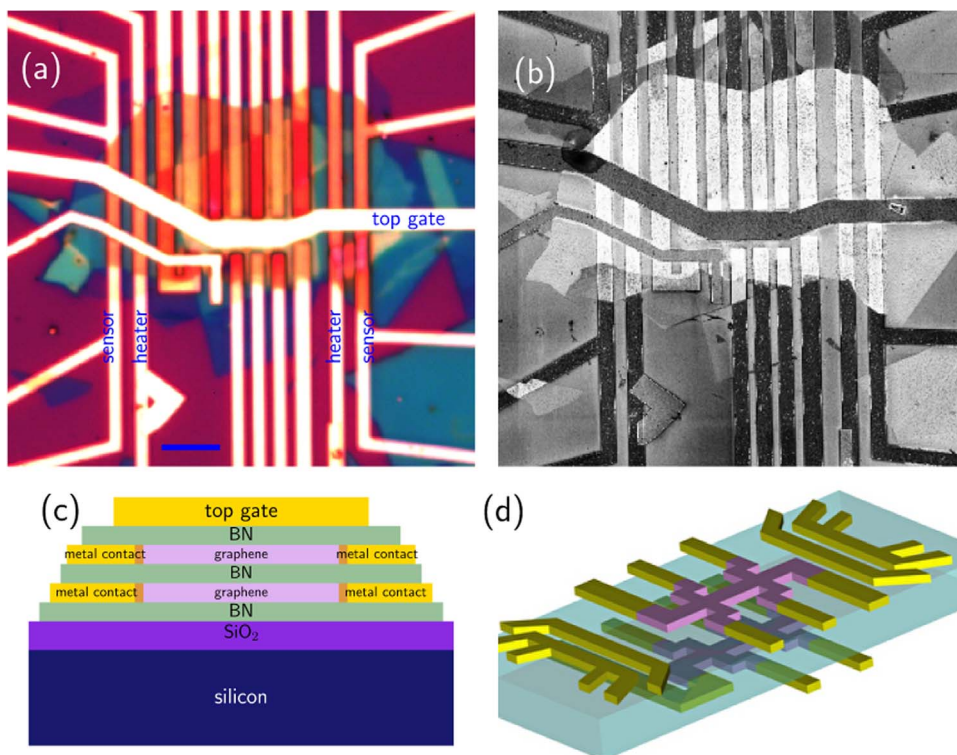
Fig. 1. Optical image (a) of the graphene device (heater lines, temperature sensors and top gate are labeled in a), the corresponding SEM image (b), the schematics of cross section (c, heaters and sensors are not shown) and the three dimensional schematics of the graphene/BN/graphene stacking with metal contacts, heaters and sensor lines (purple for graphene, yellow for metal and transparent cyan for BN). The length of the scale bar in (a) is 5 μm.

where σ is electrical conductivity, S is Seebeck coefficient, κ is thermal conductivity and T is temperature. Traditional thermoelectric units consist of two spatially separated and oppositely doped (p-type and n-type) semiconductor channel materials. The typical size of the channel materials and their separation are macroscopic, and their mutual interaction is negligible. In nanoscale thermoelectric devices, if the two channels are brought sufficiently close together, in principle the Coulomb interaction between the charge carriers in the two channels can become notable. It remains unknown how such interaction may affect the thermoelectric transport properties. Such a previous unexplored regime in thermoelectric devices may be studied in closely separated double layer systems, such as graphene/BN/graphene.

In this paper, Coulomb drag resistivity (which arises from the interlayer interaction) and counterflow Seebeck coefficient are measured in two BLG layers separated by a thin BN layer shown in Fig. 1. The Coulomb drag resistivity and Seebeck coefficient in each BLG layer show the expected sign when the carrier type in each layer is changed. In our current devices, the counterflow Seebeck coefficient can be well approximated by the sum of Seebeck coefficients from the individual layers, suggesting that the effect of the interlayer interaction on the counterflow thermoelectric transport is negligibly small (although the interlayer interaction is sufficient to give a measurable Coulomb drag signal). The magnitude of counterflow Seebeck coefficient and the calculated counterflow power factor increase with temperature. We provide a quantitative analysis about the thermoelectric performance in the counterflow regime. The maximum power factor at room temperature can be ~ 700 μW/K^{2}cm, exceeding that of the good thermoelectric material Bi$_2$Te$_3$ at least by a factor of 5 [39]. Such a high power factor could be useful in thermoelectric applications, even though ZT value is small due to high thermal conductivity of graphene. The possible impact of Coulomb drag on the counterflow Seebeck coefficient, though small in our samples, can be enhanced in devices with smaller separation between the two channels and could open new possibilities in developing high ZT thermoelectric materials and structures.

2. Methods

The measured graphene device in Fig. 1a-b consists of two BLG layers separated by a thin BN layer (~ 20 nm thick). They have isolated metal contacts, as shown by the schematics in Fig. 1c-d. The bilayer nature of graphene is confirmed by Raman spectroscopy and quantum Hall measurement. This layered structure is sitting on a local BN dielectric on SiO$_2$ (300 nm)/silicon substrate and is covered by the top gate BN dielectric and metal. To fabricate the sample, the bottom BN layer is exfoliated onto the SiO$_2$/silicon substrate. The other graphene and BN layers are subsequently transfered using a home-built flake transfer stage with an alignment precision of few micrometers. We employ the flake transfer recipe [2] based on the sacrificial poly(methyl methacrylate) (PMMA) film coated on supporting polyvinyl alcohol (PVA) layer. After transferring each graphene layer, the device is annealed in H$_2$(5%)/Ar(95%) at ambient pressure to remove the residual polymers. However PMMA residuals cannot be completely eliminated [40] and exist at the interfaces of graphene and BN. They can still slightly shift the charge neutral point and induce intralayer carrier scatterings where the interlayer scattering from polymer residual may be weak due to large thickness (~ 20 nm thick) of the spacer BN layer. Oxygen plasma etching then defines the Hall bar configuration, followed by electron beam lithography and metalization (10 nm Ti and 70 nm Au). The metal lines for the heater and temperature sensor are fabricated together with the metal contacts for the top graphene layer. The device is then covered by the top BN dielectric followed by the top gate metal deposition. The device is finally bonded onto a chip carrier and measured in cryostats. Except the study of temperature dependence, all the other measurements are carried out at room temperature.

The electrical connection to measure the counterflow Seebeck coefficient is shown in Fig. 2 where the counterflow Seebeck coefficient is specifically determined from the voltage V_S measured between two layers at the right end while they are connected at the left. The lateral temperature difference (ΔT) of ~ 1 K [41] is established between two ends in each graphene layer. The top and bottom gate voltages V_{tg} and V_{bg} can control the carrier densities of the corresponding graphene layers, e.g., the top layer of p-type and the bottom layer of n-type here
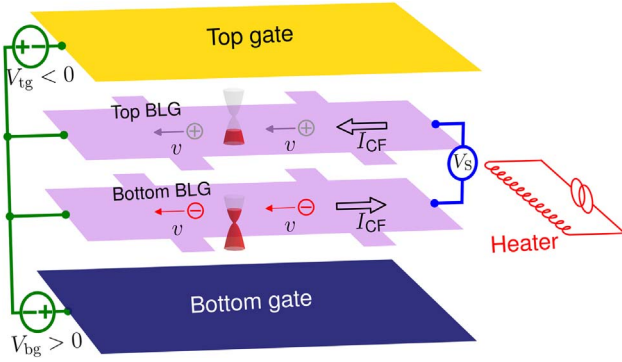
Fig. 2. Schematics of counterflow Seebeck coefficient measurement. The arrows ⟵ and ⟵ for the charge carrier symbols ⊕ and ⊖ denote the moving carriers driven by the temperature gradient created by the heater with the velocity *v* labeled below the arrows. The arrows ⟸ and ⟹ represent the counterflow electrical currents with magnitude of I_{CF} (zero at open circuit). The counterflow Seebeck voltage V_S is positive where the top (bottom) layer is p-type (n-type).

are indicated by the red filling of the parabolic band structures and the charge symbols ⊕ and ⊖.

A low frequency alternating (AC) heating current of a few milli-ampere in amplitude is applied across the heater line and the counterflow Seebeck voltage V_S (voltage drop from the top to bottom layer measured at the right ends) is then detected using a lock-in amplifier at the second harmonic (with 90° phase shift). The heater and temperature sensors are calibrated [42] to calculate the established (RMS) temperature difference ΔT [41] and convert the Seebeck voltage V_S to Seebeck coefficient $S_{CF} = V_S/\Delta T$. The sign of S_{CF} is negative when the top and bottom graphene layers are p- and n-type respectively. During measuring V_S, the resistances of both graphene layers are simultaneously measured using another two lock-in amplifiers at different lock-in frequencies. The frequencies for the three lock-in amplifiers are varied to ensure that the measured V_S and resistances are insensitive to such variations, indicating independent thermoelectric and resistance response signals in each graphene layer.

3. Results

The tunneling resistance between two graphene layers is measured to be larger than 10 GΩ, an indication of good electrical isolation between them. The color maps of intralayer resistivities ρ_t and ρ_b as functions of V_{bg} and V_{tg} for the top and bottom BLG are shown in Fig. 3a and b respectively. The solid purple line in Fig. 3a[b] is ρ_t (plotted on the right axis) vs. V_{tg} [ρ_b (plotted on the top axis) vs. V_{bg}] when $V_{bg} = 0$ [$V_{tg} = 0$]. It is obvious that the resistivity of the top [bottom] BLG layer cannot be effectively tuned by the bottom [top] gate voltage due to the strong screening by the bottom [top] BLG layer. The charge neutral point for the top [bottom] BLG layer slightly decreases as V_{bg} [V_{tg}] increases, due to the incomplete screening from the other graphene layer. The charge neutral points for both graphene layers are very close to zero gate voltage, since both graphene layers are sandwiched between two BN layers, resulting in reduced charge doping of the BLG layers.

The color map of Coulomb drag resistivity $\rho_d = V_d/(I_d N_{sq})$ vs. V_{tg} and V_{bg} is shown in Fig. 3c, where the current I_d is applied on the drive layer while the voltage V_d is measured on the drag layer and N_{sq} is the ratio of the length along which I_d is applied to the width of the graphene channel. The sign of ρ_d is defined to be positive when V_d has the same sign as the voltage drop in the drive layer when the drag layer has zero current. Various procedures (e.g., swapping the drag and drive layers, changing the grounding positions and varying the lock-in frequencies) are carried out to ensure the physical Coulomb drag signal is detected [43]. The Coulomb drag resistivity is measured at a low frequency of $f = 2.7$ Hz. The out-of-phase component of ρ_d is at least one order of magnitude smaller than the in-phase component except around Dirac

point where ρ_d is close to zero. The solid line in Fig. 3d is corresponding to the horizontal cut in Fig. 3c at $V_{bg} = -10$ V. The labels (x, y) in Fig. 3c and d where x and y can be either n or p indicate that the charge carriers of the top BLG is of x-type while that of the bottom BLG is of y-type. Though the shape of the color map is not symmetrical (probably due to charge inhomogeneity), the sign of ρ_d is correct, i.e, positive for opposite type of charge carriers in both BLG layers (x ≠ y) and negative for same type of charge carriers (x = y). Note that the regions of positive ρ_d located at the top left and bottom right quadrants are connected across the charge neutral point in both BLG layers, similar to the measurement of Coulomb drag between two single layer graphene (SLG) layers in Ref. [8]. For another sample of BLG double layers, the color map of Coulomb drag resistivity (see Fig. S2 in the Supplementary material) exhibits different behavior around the charge neutral point in both BLG layers but similar to another reported result for SLG double layers [28]. The color map of ρ_d at temperature of 240 K and 200 K can be found in Fig. S1 in the Supplementary material. Recent measurements of Coulomb drag in BLG double layers show anomalous negative drag when the carriers in both layers are of the same type at temperatures below ~ 200 K [10] and 10 K [9]. In our sample no such negative drag is observed for temperatures above 200 K. The drag resistivity is too small to allow reliable measurement of Coulomb drag signals.

The blue solid lines in Fig. 4a[b] are the measured Seebeck coefficient $S_{top[bot]}$ of the top [bottom] BLG layer tuned by the top [bottom] gate voltage $V_{tg[bg]}$ while the bottom [top] BLG layer is electrically floating. The green dashed lines are calculated from the Mott formula $S = \frac{\pi^2 k_B^2}{3e\rho} T \frac{d\rho}{dV_g} \frac{dV_g}{dE_F}$, where e is the elementary charge, k_B is the Boltzmann constant, V_g is the gate voltage, ρ is the intralayer resistivity, and E_F is the Fermi level [44]. The V_g vs. E_F relation can be obtained by evaluating the energy dispersion $E(k) = \pm \frac{1}{2}\gamma_1 [\sqrt{1 + 4v_F^2 \hbar^2 k^2/\gamma_1^2} - 1]$ (+ for conduction band and - for valence band) of BLG at the Fermi wave vector $k_F = \sqrt{\pi C_g |V_g - V_D|/e}$, where the Fermi velocity is $v_F = 10^6$ m/s, $\gamma_1 = 0.39$ eV, C_g is the gate capacitance and V_D is the gate voltage at the charge neutral point [45]. Note that the wiggles in the green dashed lines are due to the numerical computation of $\frac{d\rho}{dV_g}$ from the solid purple lines in Fig. 3a and b.

The color map of counterflow Seebeck coefficient S_{CF} (=$V_S/\Delta T$) vs. V_{tg} and V_{bg} at room temperature is shown in Fig. 4c (temperature dependence of S_{CF} can be found in Fig. S3 in the Supplementary material). Four quadrants of this color map are separated by white areas near zero gate voltages. Large magnitude of negative [positive] S_{CF} appears in the top left [bottom right] quadrant when the top and bottom graphene layers are p- and n-type [n- and p-type] respectively. In this regime where two graphene layers have different carrier types, we found that the magnitude of S_{CF} is simply the sum of the magnitude of Seebeck coefficient in each individual layer. We do not find any noticeable interlayer interaction effects on S_{CF} due to the weak Coulomb drag in our samples (ρ_d is nearly three orders of magnitude smaller than ρ_t or ρ_b). The magnitude of S_{CF} in the other two quadrants is smaller or even close to zero since the signs of Seebeck coefficient in both layers are same and they tend to cancel each other. The above discussion can be represented by the formula $S_{CF} = S_{bot} - S_{top}$ which is demonstrated in Fig. 4d-e. For example in Fig. 4d, the solid blue line is from the horizontal cut in Fig. 4c while the dashed green line is calculated from $S_{bot} - S_{top}$ where S_{bot} is the constant value taken at the red point in Fig. 4b for $V_{bg} = 45$V and S_{top} is the solid blue curve in Fig. 4a. These two lines are close to each other, validating the above formula. The small discrepancy may come from the incomplete gating screening of BLG layers, resulting in small variation of the carrier density of the top [bottom] BLG when V_{bg} [V_{tg}] is changed and V_{tg} [V_{bg}] is fixed. The horizontal lines of zero S_{CF} in Fig. 4d-e separate them into red (positive S_{CF}) and cyan (negative S_{CF}) areas. Note that the lines of S_{CF} vs. gate voltage cross zero twice, which is not possible for an isolated and homogeneous single layer of BLG. This explains that the top right and
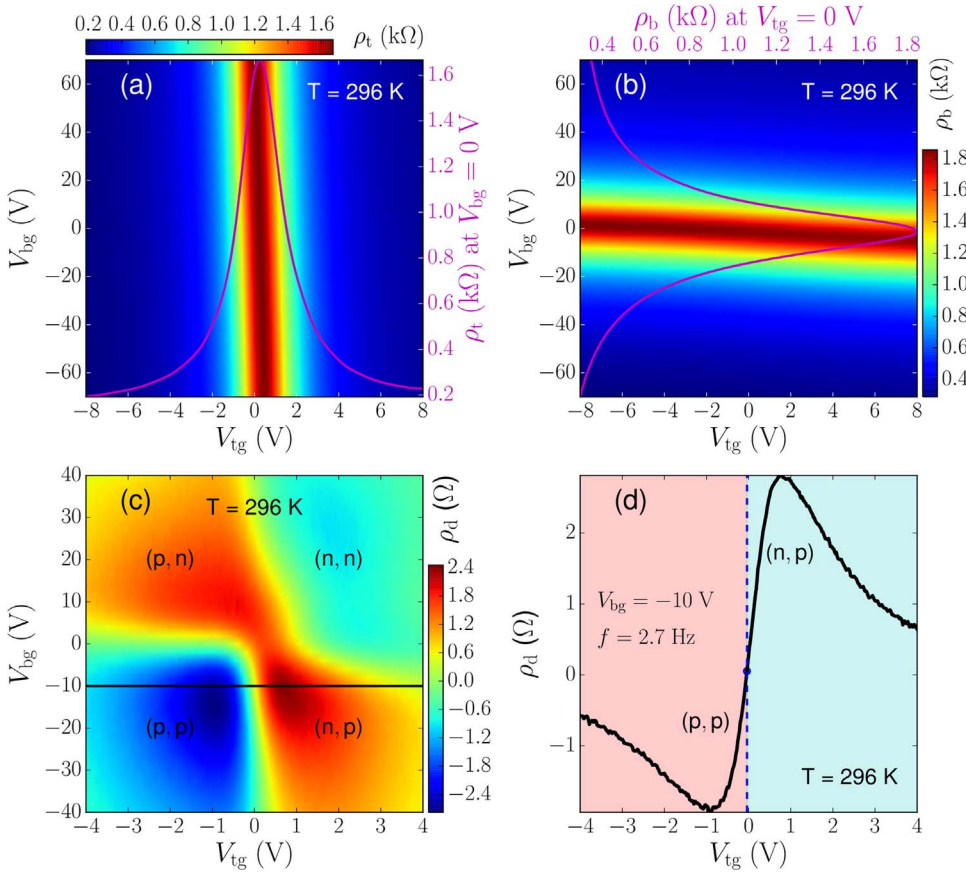
Fig. 3. Color maps (a-c) of intralayer resistivities (a) ρ_t for top BLG, (b) ρ_b for bottom BLG and Coulomb drag resistivity (c) ρ_d vs. V_{tg} and V_{bg}, and (d) ρ_d vs. V_{tg} when $V_{bg} = -10$ V. The purple line in (a) [(b)] is ρ_t vs. V_{tg} [ρ_b vs. V_{bg}] when $V_{bg} = 0$ [$V_{tg} = 0$] with the ρ_t [ρ_b] plotted at right [top]. Note that (d) is corresponding to the horizontal cut in (c). The vertical blue dashed line in (d) divides it into red and cyan regions indicating p- and n-type of top BLG. The labels (x, y) in (c) and (d) indicate the x[y]-type of charge carriers for top [bottom] BLG, where x and y can be n or p.

bottom left quadrants in Fig. 4c are composed of regions with different sign of S_{CF} and the boundaries of white line segments with zero S_{CF}.

The power factor in the counterflow thermoelectric transport regime is defined as $P = S_{CF}^2/[(\rho_t + \rho_b)t]$, where the BLG thickness t (= 0.67 nm) is introduced to allow convenient comparison of our measured results with the other experiments and calculations. Its color map is shown in Fig. 4f. Note that the gate voltages corresponding to the maximum of P are different from that of the magnitude of S_{CF} since the BLG resistivity is strongly dependent on the gate voltages. Here the extrinsic resistance mainly from the metal-graphene contacts is ignored, because it is material and process dependent and can be one order smaller than the graphene resistances after special contact treatment [46]. The maximum power factor is $P_{max} \sim$ 700 μW/K²cm. A very recent work has obtained similar power factor in graphene/BN devices [47].

The positive and negative peak values of S_{CF} vs. temperature are shown in Fig. 5a. The magnitudes of both peaks decrease with temperature. The maximum power factor P_{max} in the two regimes of opposite carrier types for the two graphene layers (solid red [dashed blue] line for top layer of n-type [p-type] and bottom layer of p-type [n-type]) vs. temperature is shown in Fig. 5b. These two lines show similar trend and manifest the symmetry between the two regimes. It is expected that P_{max} will increase further as temperature increases above room temperature. Note that the peak values of S_{CF} and P_{max} are both achieved in (p, n) and (n, p) regions, but the corresponding gate voltages are different.

4. Discussion

Although graphene has high Seebeck coefficient and electrical conductivity [49,50], hence high power factor, its ZT is small due to its high thermal conductivity [51,52]. While small ZT materials are not good candidates for thermoelectric applications, significant effort has been devoted to enhancing the ZT of graphene and related

nanostructures [53–69], usually by reducing the thermal conductivity with various methods. The high value of power factor is still promising in electricity generation at special circumstances, e.g., when space is constrained and high efficiency is not needed. The maximum output power for the thermoelectric module with N_T serially connected (see Fig. S5 in the Supplementary material) units is $Q_m = P_{max} N_T t \Delta T^2/4N_{sq}$ at the impedance match [70] where the load resistance equals to the internal resistance ($=N_T(\rho_t + \rho_b)N_{sq}$) of the module, where N_{sq} is the ratio of the length L (the length of graphene is measured along the direction of temperature gradient) to the width W and $P_{max} \sim$ 700 μW/K²cm. The expression of Q_m indicates that the effective power factor (= $N_T P_{max}$) of N_T serially connected units is proportional to N_T, useful for building high output voltage thermoelectric modules. For large N_T, the internal resistance of the module will be proportionally large and the power delivery capability will be limited when the load resistance is a constant. This issue can be resolved by reducing N_{sq}. The values of N_T and N_{sq} can be optimally chosen for any specific load resistance and power requirement.

For $\Delta T = 50$ K (e.g., the average temperature difference between the hot and cold spots in the modern CPUs), $Q_m = 2.9$ W for $1/N_{sq} = N_T = 10000$. Such serially connected thermopower generator has a thermal conductance of $G = 2\kappa N_T t/N_{sq} = 201$ W/K for $\kappa = 1500$ W/m K (G will be larger if the heat conduction channels through the insulating materials between graphene layers and the other supporting/gating materials are included), useful for applications of fast heat dissipation while generating electricity energy. Due to the low mass density of graphene, the power output per mass is as high as $\sim 1.1 \times 10^9$ W/kg (the total graphene area is $\sim$ 20 μm²) without including the mass of the insulating materials between graphene layers. It is still an extremely large number even when the mass of those insulating materials are included. For example, inserting a 3 nm thick of BN layer between graphene layers is good enough to avoid leakage between graphene layers. The mass density of BN is about 4.5 times
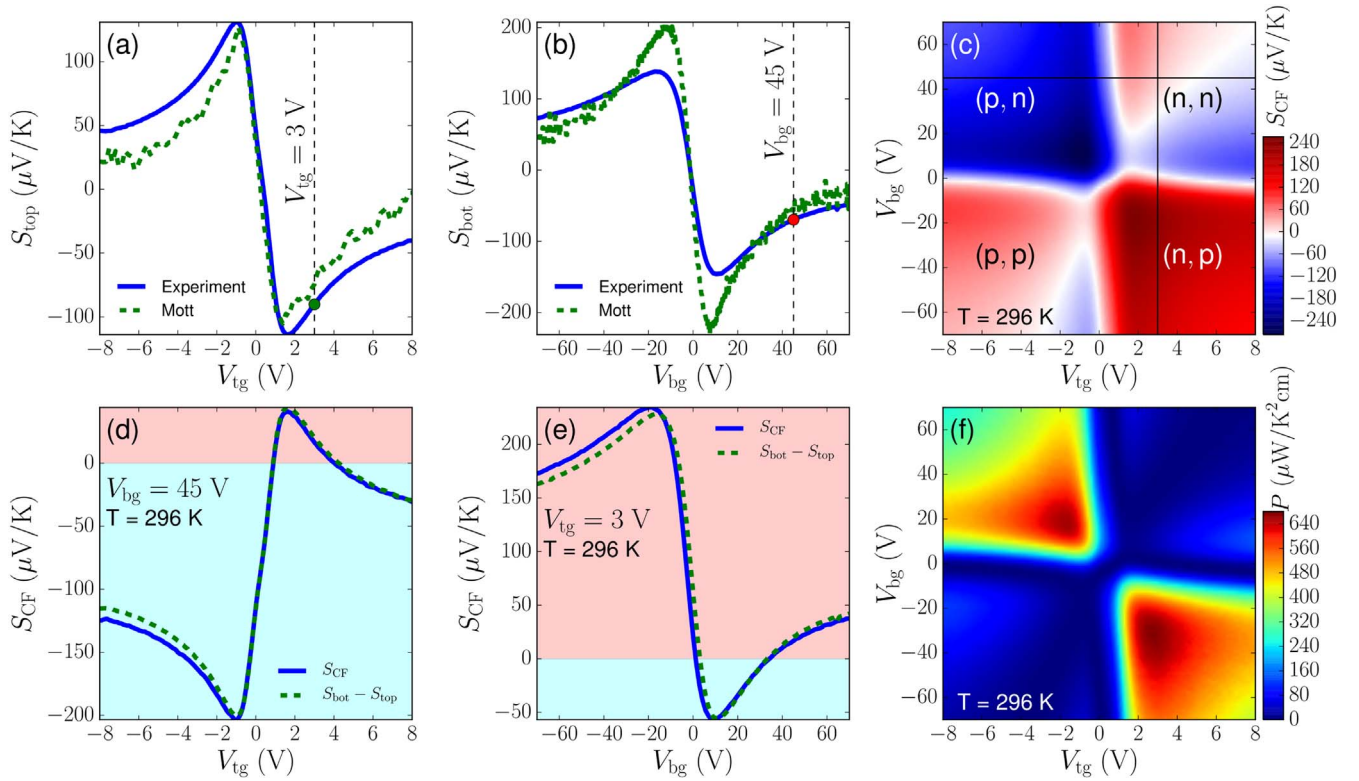
Fig. 4. Seebeck coefficient of top (a) and bottom (b) BLG layers (the green dashed lines are calculated Seebeck coefficients from Mott formula) vs. V_{tg} and V_{bg} respectively, color map (c) of counterflow Seebeck coefficient S_{CF} vs. V_{tg} and V_{bg}, (d) S_{CF} vs. V_{tg} for $V_{bg} = 45$ V, (e) S_{CF} vs. V_{bg} for $V_{tg} = 3$ V and color map (f) of power factor P vs. V_{tg} and V_{bg}. The solid blue line in (a) [(b)] is measured within the top [bottom] layer, which is connected to the bottom [top] layer as in Fig. 2 (there is no observable change in the results if two layers are disconnected). The solid blue line (measured data) in (d) [(e)] is from the horizontal [vertical] cut in (c). The dashed green line in (d) [(e)] is calculated from $S_{bot} - S_{top}$ where S_{bot} [S_{top}] is the constant value at $V_{bg} = 45$ V marked by the red dot in (b) [at $V_{tg} = 3$ V marked by the green dot in (a)] while S_{top} [S_{bot}] is the solid blue line in (a) [(b)]. The red [cyan] area in (d) and (e) represents the positive [negative] value of S_{CF}.

larger than that of graphene, thus the power output per mass is reduced to $\sim 2.4 \times 10^8$ W/kg. The mass of the other materials such as the gate metal (can be replaced by graphene or become not needed by doping graphene chemically for example) and interconnects (could be replaced by graphene) is not considered here. Such high power per mass makes graphene promising in light weight thermoelectric applications [71].

The intralayer resistivities may be affected by the interlayer Coulomb drag [72], which will affect the power factor. As seen from Fig. 3c, the maximum magnitude of ρ_d is about 2.5 Ω, much smaller than the resistivity of each graphene layer. Therefore, such Coulomb drag effect can be neglected in the counterflow thermoelectric transport measured here. It may become important when ρ_d is large, especially when it is close to the intralayer resistivities. Large Coulomb drag resistivity is an indication of strong interlayer interactions. It has been

suggested that the formation of excitons composed of electron-hole pairs where the electrons and holes reside in different layers will possibly lead to high ZT structures [73–75].

5. Conclusion

In conclusion, Coulomb drag and counterflow thermoelectric transport measurements are performed in layered structures of BN/BLG/BN/BLG/BN. The magnitude of the counterflow Seebeck coefficient exhibits a peak in the regime where two graphene layers have opposite sign of charge carriers. The maximum power factor is about 700μ W/K²cm at room temperature. A quantitative analysis indicates that graphene can be useful for light weight thermoelectric systems. The counterflow Seebeck coefficient and power factor decrease with
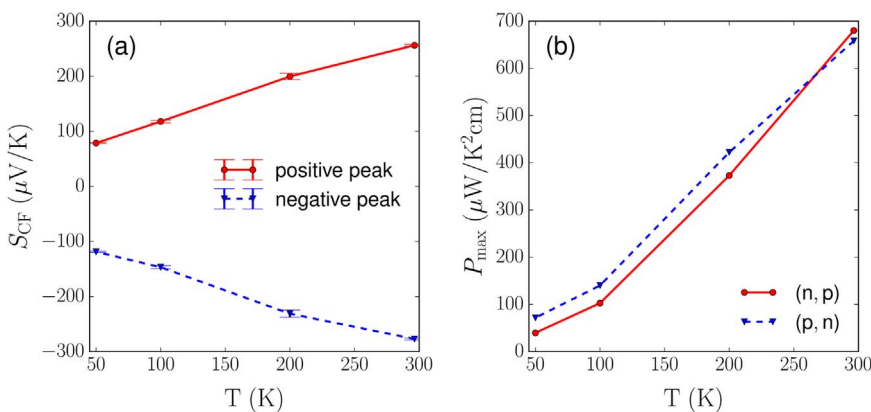

Fig. 5. Positive and negative peaks of S_{CF} (a) and the maximum power factor (b) P_{max} vs. temperature. The error bars (type A standard uncertainties [48]) in (a) mainly come from the calibration for the temperature sensors. The positive/negative peaks in S_{CF} and positive peaks in P are taken from the corresponding color maps showing their dependence on V_{tg} and V_{bg} at various temperatures.

temperature from 300 K to 50 K. The measured interlayer Coulomb drag resistivity is small ($< 3 \, \Omega$) compared to the intralayer resistivity, making negligible impact of Coulomb drag on the counterflow thermoelectric transport in the present structures. However, further reducing the separation between two BLG layers may shed light on the interplay between Coulomb drag and counterflow thermoelectric transport.

Acknowledgment

Appendix A. Supplementary data

Supplementary data associated with this article can be found in the online version at http://dx.doi.org/10.1016/j.nanoen.2017.07.035.

References

[1] C. Dean, A. Young, I. Meric, C. Lee, L. Wang, S. Sorgenfrei, K. Watanabe, T. Taniguchi, P. Kim, K. Shepard, Boron nitride substrates for high-quality graphene electronics, Nat. Nanotechnol. 5 (10) (2010) 722–726.

[2] T. Taychatanapat, K. Watanabe, T. Taniguchi, P. Jarillo-Herrero, Quantum hall effect and landau-level crossing of dirac fermions in trilayer graphene, Nat. Phys. 7 (8) (2011) 621–625.

[3] C.R. Dean, A.F. Young, P. Cadden-Zimansky, L. Wang, H. Ren, K. Watanabe, T. Taniguchi, P. Kim, J. Hone, K.L. Shepard, Multicomponent fractional quantum hall effect ingraphene, Nat. Phys. 7 (9) (2011) 693–696, http://dx.doi.org/10.1038/nphys2007.

[4] L. Britnell, R.V. Gorbachev, R. Jalil, B.D. Belle, F. Schedin, M.I. Katsnelson, L. Eaves, S.V. Morozov, N.M. Peres, Electron tunneling through ultrathin boron nitride crystalline barriers, Nano Lett. 12 (3) (2012) 1707–1710.

[5] A. Geim, I. Grigorieva, Van der waals heterostructures, Nature 499 (7459) (2013) 419–425.

[6] L. Jiao, B. Fan, X. Xian, Z. Wu, J. Zhang, Z. Liu, Creation of nanostructures with poly (methyl methacrylate)-mediated nanotransfer printing, J. Am. Chem. Soc. 130 (38) (2008) 12612–12613, http://dx.doi.org/10.1021/ja805070b.

[7] L. Jiao, X. Xian, Z. Wu, J. Zhang, Z. Liu, Selective positioning and integration of individual single-walled carbon nanotubes, Nano Lett. 9 (1) (2009) 205–209, http://dx.doi.org/10.1021/nl802779t.

[8] R. Gorbachev, A. Geim, M. Katsnelson, K. Novoselov, T. Tudorovskiy, I. Grigorieva, A. MacDonald, S. Morozov, K. Watanabe, T. Taniguchi, Strong coulomb drag and broken symmetry in double-layer graphene, Nat. Phys. 8 (12) (2012) 896–901.

[9] K. Lee, J. Xue, D.C. Dillen, K. Watanabe, T. Taniguchi, E. Tutuc, Giant frictional drag in double bilayer graphene heterostructures, Phys. Rev. Lett. 117 (2016) 046803.

[10] J. Li, T. Taniguchi, K. Watanabe, J. Hone, A. Levchenko, C. Dean, Negative coulomb drag in double bilayer graphene, Phys. Rev. Lett. 117 (2016) 046802.

[11] L. Ponomarenko, A. Geim, A. Zhukov, R. Jalil, S. Morozov, K. Novoselov, I. Grigorieva, E. Hill, V. Cheianov, V. FalKo, Tunable metal-insulator transition in double-layer graphene heterostructures, Nat. Phys. 7 (12) (2011) 958–961.

[12] T. Georgiou, R. Jalil, B.D. Belle, L. Britnell, R.V. Gorbachev, S.V. Morozov, Y.-J. Kim, A. Gholinia, S.J. Haigh, O. Makarovsky, Vertical field-effect transistor based on graphene-ws2 heterostructures for flexible and transparent electronics, Nat. Nanotechnol. 8 (2) (2013) 100–103.

[13] L. Britnell, R. Gorbachev, A. Geim, L. Ponomarenko, A. Mishchenko, M. Greenaway, T. Fromhold, K. Novoselov, L. Eaves, Resonant tunnelling and negative differential conductance in graphene transistors, Nat. Commun. 4 (2013) 1794.

[14] A. Mishchenko, J. Tu, Y. Cao, R. Gorbachev, J. Wallbank, M. Greenaway, V. Morozov, S. Morozov, M. Zhu, S. Wong, F. Whiters, C. Woods, Y. Kim, K. Watanabe, T. Taniguchi, E. Vdovin, O. Makarovsky, T. Fromhold, V. Falko, A. Geim, K. Novoselov, Twist-controlled resonant tunnelling in graphene/boron nitride/graphene heterostructures, Nat. Nanotechnol. 9 (10) (2014) 808–813.

[15] M.J. Manfra, Molecular beam epitaxy of ultra-high-quality algaas/gaas heterostructures: enabling physics in low-dimensional electronic systems, Annu. Rev. Condens. Matter Phys. 5 (1) (2014) 347–373, http://dx.doi.org/10.1146/annurev-conmatphys-031113-133905.

[16] J. Eisenstein, A. MacDonald, Bose-einstein condensation of excitons in bilayer electron systems, Nature 432 (7018) (2004) 691–694.

[17] H. Min, R. Bistritzer, J.-J. Su, A. MacDonald, Room-temperature superfluidity in graphene bilayers, Phys. Rev. B 78 (12) (2008) 121401.

[18] Y.E. Lozovik, A. Sokolik, Electron-hole pair condensation in a graphene bilayer, JETP Lett. 87 (1) (2008) 55–59.

[19] M.Y. Kharitonov, K.B. Efetov, Electron screening and excitonic condensation in double-layer graphene systems, Phys. Rev. B 78 (24) (2008) 241401.

[20] C.-H. Zhang, Y.N. Joglekar, Excitonic condensation of massless fermions in graphene bilayers, Phys. Rev. B 77 (23) (2008) 233405.

[21] Y.E. Lozovik, S. Ogarkov, A. Sokolik, Condensation of electron-hole pairs in a two-layer graphene system: correlation effects, Phys. Rev. B 86 (4) (2012) 045429.

[22] D. Abergel, R. Sensarma, S.D. Sarma, Density fluctuation effects on the exciton condensate in double-layer graphene, Phys. Rev. B 86 (16) (2012) 161412.

[23] I. Sodemann, D. Pesin, A. MacDonald, Interaction-enhanced coherence between two-dimensional dirac layers, Phys. Rev. B 85 (19) (2012) 195136.

[24] Y.F. Suprunenko, V. Cheianov, V.I. Fal'ko, Phases of the excitonic condensate in two-layer graphene, Phys. Rev. B 86 (15) (2012) 155405.

[25] A. Perali, D. Neilson, A.R. Hamilton, High-temperature superfluidity in double-bilayer graphene, Phys. Rev. Lett. 110 (14) (2013) 146803.

[26] D. Abergel, M. Rodriguez-Vega, E. Rossi, S.D. Sarma, Interlayer excitonic superfluidity in graphene, Phys. Rev. B 88 (23) (2013) 235402.

[27] D. Nandi, A. Finck, J. Eisenstein, L. Pfeiffer, K. West, Exciton condensation and perfect coulomb drag, Nature 488 (7412) (2012) 481–484.

[28] S. Kim, E. Tutuc, Coulomb drag and magnetotransport in graphene double layers, Solid State Commun. 152 (15) (2012) 1283–1288.

[29] X. Liu, K. Watanabe, T. Taniguchi, B. I. Halperin, P. Kim, Quantum Hall Drag of Exciton Superfluid in Graphene, arXiv:1608.03726.

[30] J. Li, T. Taniguchi, K. Watanabe, J. Hone, C. Dean, Excitonic Superfluid Phase in Double Bilayer Graphene, arXiv:1608.05846.

[31] C. Goupil, W. Seifert, K. Zabrocki, E. Müller, G.J. Snyder, Thermodynamics of thermoelectric phenomena and applications, Entropy 13 (8) (2011) 1481–1517.

[32] D.M. Rowe, Thermoelectrics Handbook: Macro to Nano, CRC Press, 2005.

[33] S. Lin, P. Tong, B. Wang, S. Lin, Y. Huang, Y. Sun, Good thermoelectric performance in strongly correlated system sncco3 with antiperovskite structure, Inorg. Chem. 53 (7) (2014) 3709–3715.

[34] J. Clarke, S. Freake, Superconducting fountain effect, Phys. Rev. Lett. 29 (9) (1972) 588.

[35] T. Karpiuk, B. Grémaud, C. Miniatura, M. Gajda, Superfluid fountain effect in a bose-einstein condensate, Phys. Rev. A 86 (3) (2012) 033619.

[36] A. Rançon, C. Chin, K. Levin, Bosonic thermoelectric transport and breakdown of universality, New J. Phys. 16 (11) (2014) 113072.

[37] G.J. Snyder, E.S. Toberer, Complex thermoelectric materials, Nat. Mater. 7 (2) (2008) 105–114.

[38] M.S. Dresselhaus, G. Chen, M.Y. Tang, R. Yang, H. Lee, D. Wang, Z. Ren, J.-P. Fleurial, P. Gogna, New directions for low-dimensional thermoelectric materials, Adv. Mater. 19 (8) (2007) 1043–1053.

[39] S.V. Ovsyannikov, V.V. Shchennikov, G.V. Vorontsov, A.Y. Manakov, A.Y. Likhacheva, V.A. Kulbachinskii, Giant improvement of thermoelectric power factor of bi 2 te 3 under pressure, J. Appl. Phys. 104 (5) (2008) 053713.

[40] Y.-C. Lin, C.-C. Lu, C.-H. Yeh, C. Jin, K. Suenaga, P.-W. Chiu, Graphene annealing: how clean can it be? Nano Lett. 12 (1) (2011) 414–419.

[41] Here 1 K is the RMS Value of the Temperature Difference ΔT That is Oscillating with a Frequency of 2ω When an AC Current with Frequency ω is Applied to the Heater. ΔT is Extracted from the Measured 2ω Voltages with 90° Phase Shift on the Sensors.

[42] J.P. Small, K.M. Perez, P. Kim, Modulation of thermoelectric power of individual carbon nanotubes, Phys. Rev. Lett. 91 (2003) 256801, http://dx.doi.org/10.1103/PhysRevLett.91.256801.

[43] K. Das Gupta, A. Croxall, J. Waldie, C. Nicoll, H. Beere, I. Farrer, D. Ritchie, M. Pepper, Experimental progress towards probing the ground state of an electron-hole bilayer by low-temperature transport, Adv. Condens. Matter Phys. 2011.

[44] S.-G. Nam, D.-K. Ki, H.-J. Lee, Thermoelectric transport of massive dirac fermions in bilayer graphene, Phys. Rev. B 82 (24) (2010) 245416.

[45] E. McCann, V.I. Fal'ko, Landau-level degeneray and quantum hall effect in a graphite bilayer, Phys. Revi. Lett. 96 (8), p. 086805.

[46] W.S. Leong, H. Gong, J.T. Thong, Low-contact-resistance graphene devices with nickel-etched-graphene contacts, ACS Nano 8 (1) (2013) 994–1001.

[47] J. Duan, X. Wang, X. Lai, G. Li, K. Watanabe, T. Taniguchi, M. Zebarjadi, E.Y. Andrei, High thermoelectricpower factor in graphene/hbn devices, Proc. Natl. Acad. Sci. USA 113 (50) (2016) 14272–14276.

[48] BIPM, IEC, IFCC, ILAC, IUPAC, IUPAP, ISO, OIML, Evaluation of measurement data – guide for expression of uncertainty in measurement, Tech. Rep., Joint Committee for Guides in Metrology, 2008.

[49] J.-H. Chen, C. Jang, S. Xiao, M. Ishigami, M.S. Fuhrer, Intrinsic and extrinsic performance limits of graphene devices on SiO2, Nat. Nanotechnol. 3 (4) (2008) 206–209.

[50] N. Sankeshwar, S. Kubakaddi, B. Mulimani, Thermoelectric Power in Graphene, 9 Intech, 2013, pp. 1–56.

[51] A.A. Balandin, Thermal properties of graphene and nanostructured carbon materials, Nat. Mater. 10 (8) (2011) 569–581.

[52] E. Pop, V. Varshney, A.K. Roy, Thermal properties of graphene: fundamentals and applications, MRS Bull. 37 (12) (2012) 1273–1281.

[53] H. Sevinçli, G. Cuniberti, Enhanced thermoelectric figure of merit in edge-disordered zigzag graphene nanoribbons, Phys. Rev. B 81 (11) (2010) 113401.

[54] Y. Chen, T. Jayasekera, A. Calzolari, K. Kim, M.B. Nardelli, Thermoelectric properties of graphene nanoribbons, junctions and superlattices, J. Phys.: Condens. Matter 22 (37) (2010) 372202.

[55] F. Mazzamuto, V. Hung Nguyen, Y. Apertet, C. Caër, C. Chassat, J. Saint-Martin, P. Dollfus, Enhanced thermoelectric properties in graphene nanoribbons by resonant tunneling of electrons, Phys. Rev. B 83 (2011) 235426, http://dx.doi.org/10.1103/PhysRevB.83.235426.

[56] W. Huang, J.-S. Wang, G. Liang, Theoretical study on thermoelectric properties of kinked graphene nanoribbons, Phys. Rev. B 84 (4) (2011) 045410.

[57] T. Gunst, T. Markussen, A.-P. Jauho, M. Brandbyge, Thermoelectric properties of finite graphene antidot lattices, Phys. Rev. B 84 (15) (2011) 155449.

[58] L. Liang, E. Cruz-Silva, E.C. Girão, V. Meunier, Enhanced thermoelectric figure of merit in assembled graphene nanoribbons, Phys. Rev. B 86 (11) (2012) 115438.

[59] H. Zheng, H. Liu, X. Tan, H. Lv, L. Pan, J. Shi, X. Tang, Enhanced thermoelectric performance of graphene nanoribbons, Appl. Phys. Lett. 100 (9) (2012) 093104.

[60] Z.-X. Xie, L.-M. Tang, C.-N. Pan, K.-M. Li, K.-Q. Chen, W. Duan, Enhancement of thermoelectric properties in graphene nanoribbons modulated with stub structures, Appl. Phys. Lett. 100 (7) (2012) 073105.

[61] G. Kliros, P. Divari, Thermoelectric properties of gated graphene ribbons in the ballistic regime, Superlattices Microstruct. 52 (2) (2012) 221–233.

[62] K. Yang, Y. Chen, R. D'Agosta, Y. Xie, J. Zhong, A. Rubio, Enhanced thermoelectric properties in hybrid graphene/boron nitride nanoribbons, Phys. Rev. B 86 (2012) 045425, http://dx.doi.org/10.1103/PhysRevB.86.045425.

[63] H. Karamitaheri, N. Neophytou, M. Pourfath, R. Faez, H. Kosina, Engineering enhanced thermoelectric properties in zigzag graphene nanoribbons, J. Appl. Phys. 111 (5) (2012) 054501.

[64] P.-H. Chang, B.K. Nikolić, Edge currents and nanopore arrays in zigzag and chiral graphene nanoribbons as a route toward high-z t thermoelectrics, Phys. Rev. B 86 (4) (2012) 041406.

[65] C.-N. Pan, Z.-X. Xie, L.-M. Tang, K.-Q. Chen, Ballistic thermoelectric properties in graphene-nanoribbon-based heterojunctions, Appl. Phys. Lett. 101 (10) (2012) 103115.

[66] H. Sevinçli, C. Sevik, T. Çağın, G. Cuniberti, A bottom-up route to enhance thermoelectric figures of merit in graphene nanoribbons, Sci. Rep. 3.

[67] P.S.E. Yeo, M.B. Sullivan, K.P. Loh, C.K. Gan, First-principles study of the thermoelectric properties of strained graphene nanoribbons, J. Mater. Chem. A 1 (36) (2013) 10762–10767.

[68] B. Feng, J. Xie, G. Cao, T. Zhu, X. Zhao, Enhanced thermoelectric properties of p-type cosb 3/graphene nanocomposite, J. Mater. Chem. A 1 (42) (2013) 13111–13119.

[69] H. Chen, C. Yang, H. Liu, G. Zhang, D. Wan, F. Huang, Thermoelectric properties of cuinte 2/graphene composites, CrystEngComm 15 (34) (2013) 6648–6651.

[70] Y. Apertet, H. Querdane, C. Goupil, P. Lecoeur, Optimal working conditions for thermoelectric generators with realistic thermal coupling, Europhys. Lett. 97 (2012) 28001.

[71] K. Yazawa, A. Shakouri, Cost-efficiency trade-off and the design of thermoelectric power generators, Environ. Sci. Technol. 45 (17) (2011) 7548–7553.

[72] E. Tutuc, M. Shayegan, D. Huse, Counterflow measurement in strongly correlated gaas hole bilayers: evidence for electron-hole pairing, Phys. Rev. Lett. 93 (3) (2004) 036802.

[73] K. Wu, L. Rademaker, J. Zaanen, Bilayer excitons in two-dimensional nanostructures for greatly enhanced thermoelectric efficiency, Phys. Rev. Appl. 2 (2014) 054013.

[74] Y. Chen, Surface Excitonic Thermoelectric Devices, US Patent App. 13/312,986, Jun. 7, 2012. 〈http://www.google.com/patents/US20120138115〉.

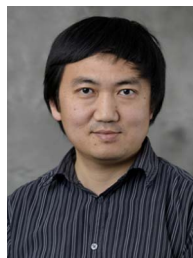[75] J. Hu, D. B. Newell, Y. Chen, (Unpublished).

Jifa Tian received his Ph.D. degree in Institute of Physics (IOP), Chinese Academy of Sciences. He is currently a postdoc working at Purdue University, West Lafayette, IN, USA.
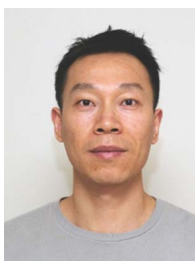

Nikolai N. Klimov received the B.S. and M.S. degrees in Physics and Applied Mathematics from the Moscow Institute of Physics and Technology (MIPT), Russia, and the Ph.D. degree in Experimental Condensed Matter Physics from Rutgers University, New Jersey, USA. He is currently an Assistant Research Scientist at the Joint Quantum Institute, University of Maryland, Maryland, USA. He also works as a Guest Research Scientist at the National Institute of Standards and Technology in Gaithersburg, Maryland.

David Newell received the B.S. and B.A. degrees in physics and mathematics, respectively, from the University of Washington, Seattle, in 1986 and the Ph.D. degree in physics from the University of Colorado, Boulder, in 1994. He is a physicist at the National Institute of Standards and Technology in Gaithersburg, Maryland, and chair of the CODATA Task Group on Fundamental Constants.

Jiuning Hu received B.S. and M.S. degrees in Electronic Engineering and Microelectronics from Tsinghua University, China, and a Ph.D. in Electrical and Computer Engineering from Purdue University. He is currently working at National Institute of Standards and Technology in Gaithersburg, Maryland.

Yong P. Chen received the M.Sc. degree in mathematics from the Massachusetts Institute of Technology, Cambridge, MA, USA, and the Ph.D. degree in electrical engineering from Princeton University, Princeton, NJ, USA. He is currently Professor of Physics and Astronomy and Electrical and Computer Engineering with Purdue University, West Lafayette, IN, USA.

Tailung Wu received his Ph.D. degree in University at Buffalo, New York. He is currently a postdoc working at Purdue University, West Lafayette, IN, USA.